CHAPTER-2

Characterization Techniques

2.1. Characterization techniques

The synthesized materials underwent comprehensive characterization techniques to gain a deeper understanding of their structural, chemical, thermal, and electrochemical properties. Fourier transform infrared spectroscopy (FTIR) was employed to analyze the infrared spectra, facilitating the identification of functional groups and chemical bonding within the material. X-ray diffraction (XRD) was utilized to determine the crystallographic structure, providing valuable insights into the phase composition and degree of crystallinity of the synthesized samples. Raman spectroscopy was used to examine vibrational modes, offering additional structural and compositional insights, particularly for cobalt-based materials and metal oxides. X-ray photoelectron spectroscopy (XPS) further provided detailed information on the chemical states and electronic structure of surface elements, enabling an in-depth understanding of the oxidation states and bonding configurations. The morphological characteristics, including surface texture and structural features, were analyzed through high-resolution imaging using field-emission scanning electron microscopy (FE-SEM), and high-resolution transmission electron microscopy (HR-TEM). Additionally, energy-dispersive spectroscopy (EDS) combined with elemental mapping enabled a quantitative analysis of the material's elemental composition and distribution, offering a comprehensive understanding of its chemical makeup.

Electrochemical characterization of the synthesized catalysts was carried out using chronopotentiometry (CP), linear sweep voltammetry (LSV), cyclic voltammetry (CV), and electrochemical impedance spectroscopy (EIS). LSV, which measures current density as a function of applied potential, was employed to assess the oxygen evolution reaction (OER) performance of the catalysts, providing key information on their electrocatalytic activity. In

contrast, CV was utilized to examine the redox behavior and catalytic activity over multiple cycles, offering insights into the stability and efficiency of the material under repeated electrochemical reactions. EIS played a crucial role in investigating the charge transfer resistance and reaction kinetics, enabling a deeper understanding of the electrode-electrolyte interface and the efficiency of electron transport during OER. Furthermore, CP, which monitors the variation in potential over time at a constant current density, was used to evaluate the long-term stability and durability of the electrocatalyst under operational conditions. Through this multi-faceted characterization approach, a thorough understanding of the material's physicochemical properties and electrochemical behavior was achieved, aiding in the optimization of its performance for catalytic applications.

To achieve a thorough characterization strategy for advanced materials research, each of these techniques is explored in depth, providing a strong foundation in their principles, applications, and importance in evaluating the overall properties and performance of the synthesized electrocatalysts.

2.2. Structural Analysis

2.2.1. Fourier transform infrared spectroscopy (FT-IR)

Fourier Transform Infrared Spectroscopy (FT-IR) is a widely used analytical technique for identifying and characterizing molecular structures based on their vibrational transitions when exposed to infrared radiation. The material preferentially absorbs wavelengths with energies that coincide with the vibrational frequencies of the molecular bonds when it is subjected to infrared light in the 4000-400 cm^{-1} range. The bending, twisting, and stretching motions

associated with the absorption of particular infrared wavelengths provide the characteristic frequencies. According to Hooke's Law, which can be expressed by following **Equation 2.1**:

$$v = (1/2\pi)\times\sqrt{(k/\mu)} \qquad \textbf{(2.1)}$$

Where, v is the vibrational frequency,

k is the bond force constant (a measure of bond strength),

μ is the reduced mass of the two atoms involved in the vibration.

The term μ could be defined mathematically by the following **Equation 2.2**:

$$M = (m_1m_2)/(m_1+m_2) \qquad \textbf{(2.2)}$$

Where, m_1 and m_2 are masses of the two atoms involved.

Higher wavenumber absorptions are the result of higher vibrational frequencies caused by lighter atoms (lower μ) and stronger bonds (higher k) [1]. FT-IR generates a unique spectral fingerprint for each molecule since every chemical bond has a different force constant and atomic mass, which makes it incredibly useful for material identification.

We investigated the functional groups of the materials synthesized in this study using the Thermo Scientific Nicolet 6700 FT-IR spectrometer **(Figure 2.1 (a))**. FT-IR spectroscopy differs from conventional dispersive infrared spectroscopy in that it relies heavily on the Michelson interferometer **(Figure 2.1 (b)).** This works in the 450–4000 cm^{-1} spectral region. The detector converts the infrared radiation into an electrical signal, which is subsequently processed using Fourier Transform mathematical algorithms to generate an absorption spectrum**.** This final spectrum represents the intensity of absorption as a function of

wavenumber (cm^{-1}), providing information about the molecular composition and chemical structure of the sample.

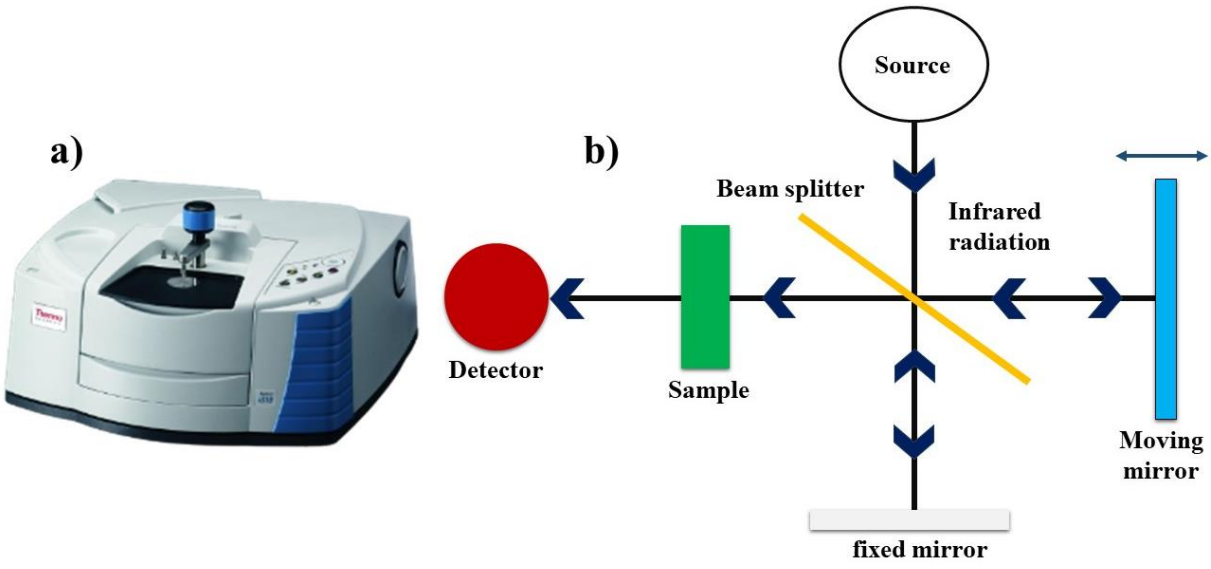

Figure 2.1 (a) Image of FT-IR spectrometer, **(b)** Michelson interferometer's operating principle.

2.2.2. X-Ray diffraction patterns (XRD)

X-ray diffraction (XRD) is a powerful and non-destructive analytical technique used to determine materials' crystallographic structure, phase composition, and microstructural properties. The fundamental idea of constructive interference of monochromatic X-rays with a crystalline substance serves as its basis. Bragg's Law states that constructive interference happens when the path difference between the scattered waves meets the condition according to the following **Equation 2.3:**

$$n\lambda = 2d \sin \theta \qquad \textbf{(2.3)}$$

Where, n is the order of reflection,

λ is the X-ray wavelength,

d is the interplanar spacing,

θ is the diffraction angle [2].

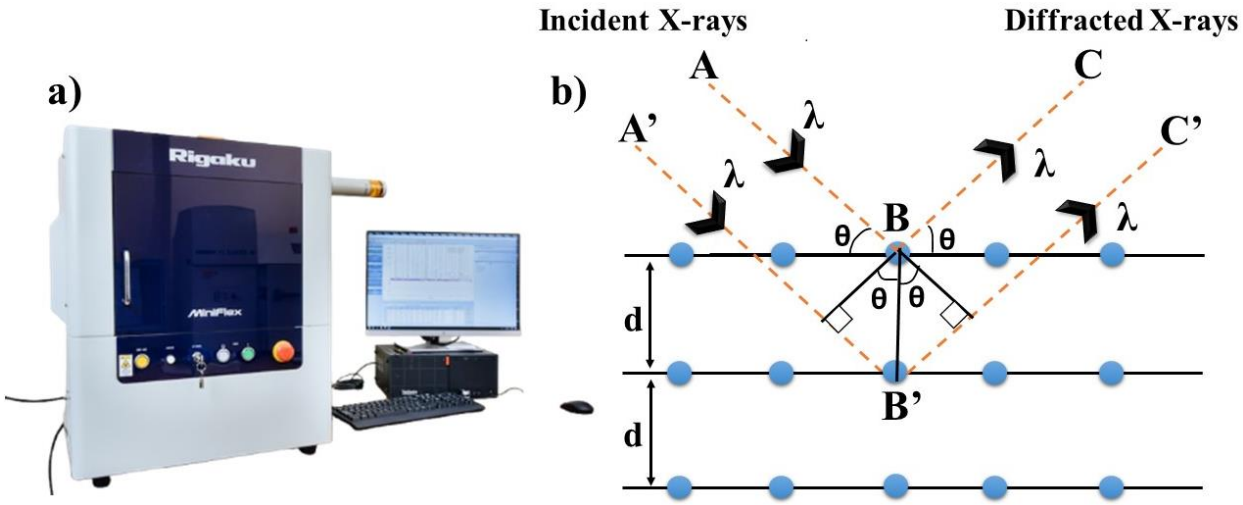

Figure 2.2 (a) Image of Rigaku Miniflex 600 diffractometer, **(b)** schematic illustration of X-ray beam diffraction through a crystalline material.

An incoming X-ray beam is dispersed in particular directions depending on the arrangement of atoms when it interacts with a crystal lattice **(Figure 2.2 (b))**. The resultant diffraction pattern offers a distinct fingerprint of the substance, enabling structural investigation, phase identification, and lattice parameter calculation [3]. Recent XRD systems use sophisticated methods like high-resolution XRD (HR-XRD) for sample analysis and Rietveld refinement for accurate structural prediction. To identify distinct lattice planes, a complete set of diffraction data is obtained by scanning the sample over a range of 2θ angles. When detectors evaluate diffracted X-rays, they produce a series of diffraction peaks that are

specific to each material and match up with certain d-spacings. Comparing these diffraction patterns to reference standards can help determine the material's phase and crystallographic structure.

The materials were analyzed using a Rigaku Miniflex 600 X-ray Diffractometer **(Figure 2.2 (a))** using Cu-Kα radiation (λ = 1.5405). Using a step size of 3 º/min, XRD data were collected throughout a 2θ range of 10-80 º with changes made as needed.

2.2.3. Raman Spectroscopy

Raman spectroscopy is a non-destructive technique used to analyze the vibrational modes, and structural properties of materials based on inelastic scattering of monochromatic light. Most photons in a laser encounter with a material undergo Rayleigh scattering, also known as elastic scattering. However, a tiny percentage of photons undergo Raman scattering, an energy shift brought on by interactions with molecular vibrations. The resulting Raman spectrum provides a fingerprint of the material, revealing information about chemical bonds, crystallinity, and molecular interactions. This technique may be employed to assess a variety of samples, including solid, powder, organic, inorganic, biological, alloy materials, etc. Raman spectra were recorded using a Renishaw **(Figure 2.3 (a))**, UK, micro-Raman system with a 2400 line-per-mm grating and Peltier-cooled CCD [4].

First, a monochromatic laser source (commonly in the visible, near-infrared, or near-ultraviolet range) is directed onto the sample. The laser light interacts with the molecules in the sample, and a very small portion of the scattered light undergoes Raman scattering. This scattered light is collected and directed through optical components such as mirrors and lenses toward a spectrometer. To eliminate the intense Rayleigh scattered light (which is at the same

wavelength as the incident laser), a notch or edge filter is used. The remaining Raman-scattered light is dispersed by a diffraction grating within the spectrometer, separating it into its component wavelengths. Finally, a sensitive detector, typically a charge-coupled device (CCD), records the intensity of the scattered light at different wavelengths **(Figure 2.3 (b))**. The resulting Raman spectrum displays intensity vs. Raman shift (in cm^{-1}), revealing vibrational information about the molecular structure of the sample.

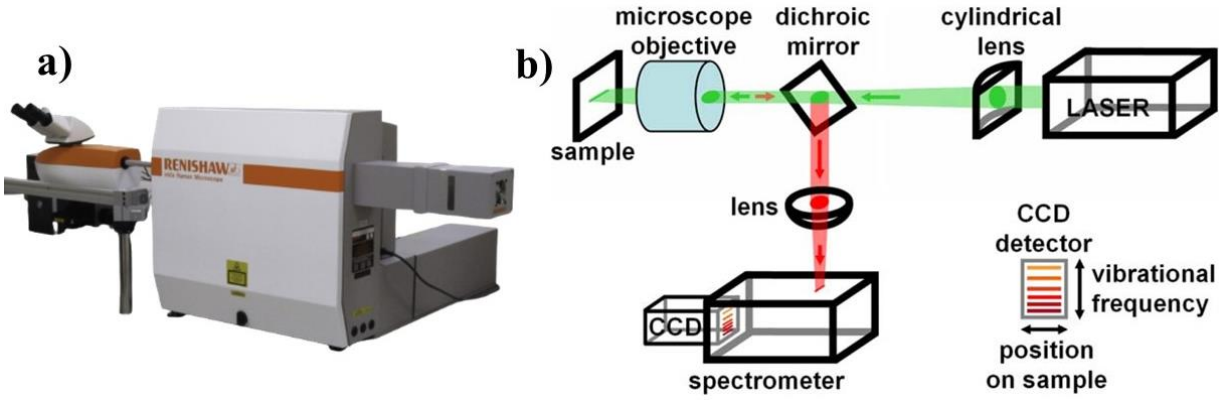

Figure 2.3 (a) Image of Raman Spectrophotometer, **(b)** schematic illustration of Raman scattering [5].

2.3. Morphological Analysis

2.3.1. Field-Emission Scanning Electron Microscopy (FE-SEM)

Field-Emission Scanning Electron Microscopy (FE-SEM) is a high-resolution imaging technique used to analyze the surface morphology, and microstructural features of materials at the nanometer scale. It works using the basic idea of electron-matter interactions, in which a field emission gun (FEG) emits a concentrated beam of high-energy electrons that are then

scanned across a sample's surface [6]. The sample and the electron beam interact to produce signals with distinctive X-rays that provide details about the composition, texture, and distribution of elements on the surface. A very coherent and narrow electron beam is produced by using a field emission source rather than a standard thermionic electron gun, as in traditional SEM. This leads to greater image contrast, less beam divergence, and much better spatial resolution.

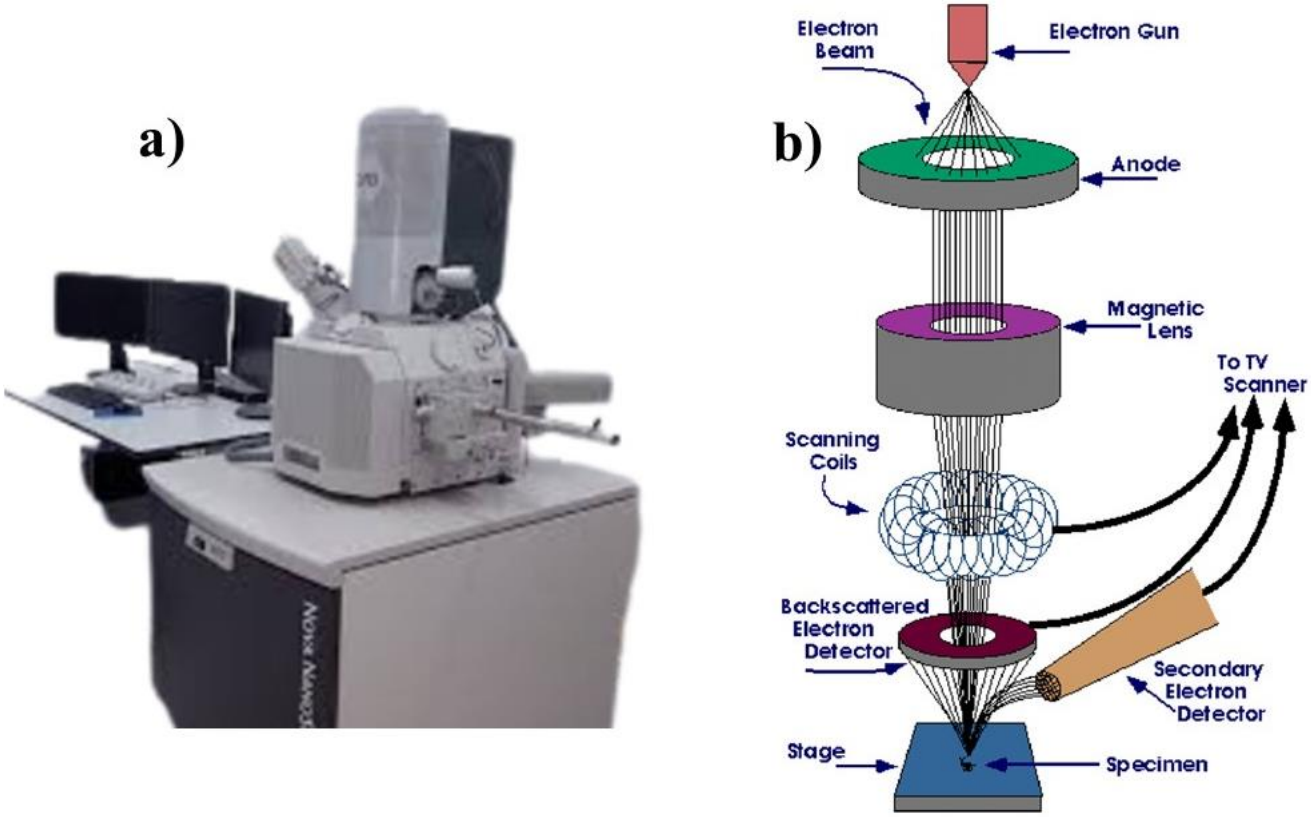

Figure 2.4 (a) Image of FE-SEM instrument, **(b)** components of the instrument [7].

The key benefit of FE-SEM over traditional SEM is its higher resolution, which is usually between 1 and 2 nm. This makes it perfect for analyzing biological specimens, thin films, nanomaterials, and microelectronic devices. Essential parts of the instrument include an

electron column with a FEG source (usually a tungsten or LaB_6 emitter), electromagnetic lenses for beam focusing, a scanning system for rastering the beam across the sample, several detectors for detecting various signals, and a vacuum system to stop electron scattering **(Figure 2.4 (b))** [8].

For our research, we employed a state-of-the-art FE-SEM manufactured in the USA, the FEI NOVA NANO SEM 450 type. We were able to thoroughly evaluate the surface features of our samples, courtesy of this apparatus **(Figure 2.4 (a))**, which ensured that even the smallest structural details were accurately noted and analyzed.

2.3.2. High-Resolution Transmission Electron Microscopy (HR-TEM)

High-Resolution Transmission Electron Microscopy (HR-TEM) is an advanced imaging and characterization technique widely used in materials science, nanotechnology, and biological research to investigate the atomic-scale structure of materials. This type of transmission electron microscopy is specialized and has a sub-nanometer spatial resolution, frequently surpassing 0.1 nm. HR-TEM is an essential technique for researching defects, interfaces, grain boundaries, and phase transitions at the atomic level because it allows direct imaging of atomic arrangements in both crystalline and amorphous materials. HR-TEM works by passing a high-energy electron beam (usually 80–300 keV) through an ultra-thin specimen, creating an interference pattern that is processed to create high-resolution images [9].

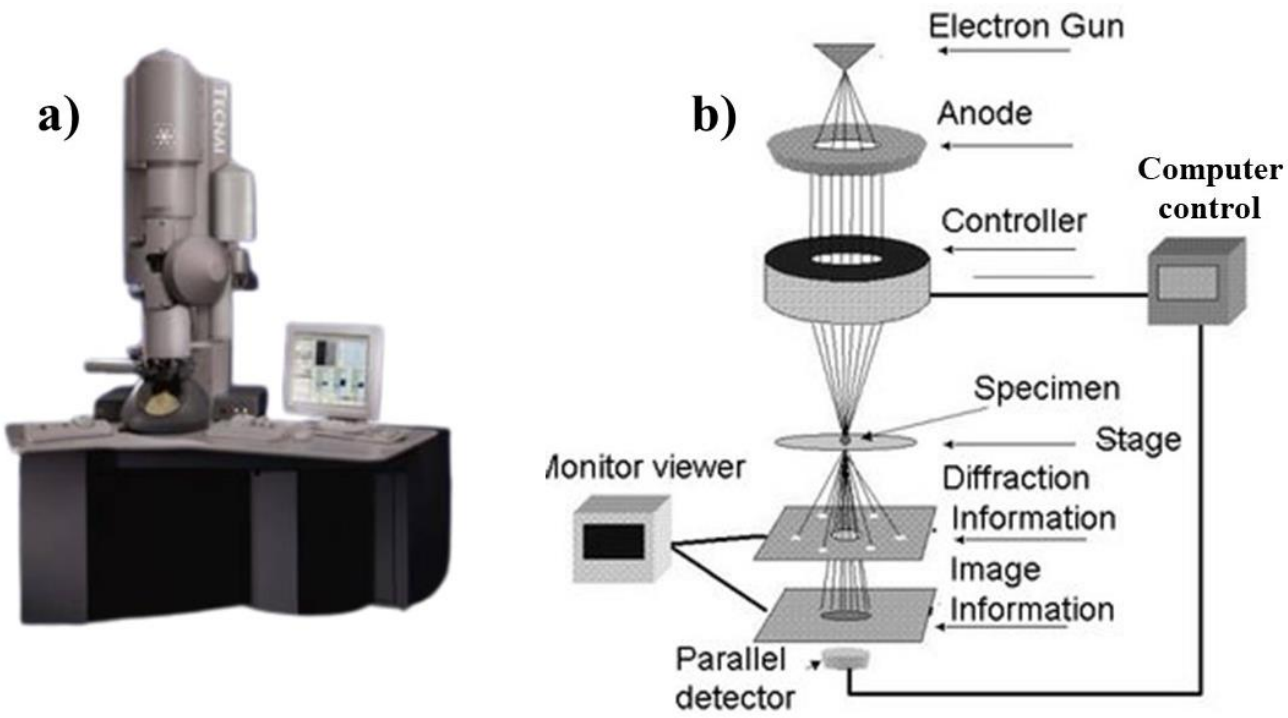

Figure 2.5 (a) HR-TEM instrument, **(b)** schematic diagram illustrating the components of a TEM microscope [10].

The working principle of HR-TEM is based on the wave nature of electrons and their interaction with the sample. An interference pattern containing structural information is produced when the electron beam travels through a thin object due to diffraction and phase contrast phenomena. After that, this pattern is enlarged and shown on a high-sensitivity camera or fluorescent screen. Phase contrast imaging is one of the primary imaging modalities in HR-TEM. This results from the interference of scattered and unscattered electron waves. HR-TEM is very useful for examining lattice structures, and crystal defects because it enables the direct viewing of atomic columns in crystalline structures.

A typical HR-TEM setup includes an electron gun (usually a field emission gun for high coherence and brightness), an imaging system like a direct electron detector or a charge-coupled device (CCD) camera, an objective aperture to improve contrast, a system of electromagnetic lenses for focusing and magnification, and a sample holder that can tilt and rotate for orientation studies **(Figure 2.5 (b))**. The electrons' interactions with different parts of the material result in variations in electron density, which are then translated into contrast on the imaging screen. This contrast reveals fine details of the sample's internal structure because denser sections seem darker due to increased electron absorption, while less dense parts allow more electrons to pass through and appear lighter [11]. In this study, HR-TEM was performed using a Tecnai G^2 20 TWIN system from FEI Company, USA (S.E.A. PTE, LTD.) **(Figure 2.5 (a))**.

2.3.3. Selected Area Electron Diffraction Patterns (SAED)

From TEM, Selected Area Electron Diffraction (SAED) is a potent characterization method used to examine the nanoscale crystallographic structure of materials. It depends on the basic ideas of electron diffraction, in which a crystalline sample is exposed to a highly concentrated electron beam, resulting in a diffraction pattern that reveals details about the material's phase composition, lattice spacing, and symmetry. SAED enables targeted diffraction examination within certain portions of a thin sample, usually on the scale of nanometers to micrometers in size, in contrast to standard XRD, which analyzes bulk materials. Because of this, SAED is especially useful for researching nanoscale flaws, polycrystalline structures, and heterogeneous materials.

For single-crystal or well-aligned crystalline materials, SAED patterns often take the shape of discrete spots, each of which represents a unique set of crystallographic planes. The distance between these spots and the atomic plane spacing are related, and the pattern's symmetry may provide details about the crystal structure (such as whether it is cubic, hexagonal, or tetragonal). We may ascertain the lattice parameters and the crystal structure of the material by examining the location and intensity of the spots. On the other hand, polycrystalline or nanocrystalline rocks form SAED patterns that seem like concentric rings. Each ring corresponds to a certain family of planes and shows the average orientation of many randomly oriented small crystals. By calculating the d-spacing of these planes using the radii of the rings, one may ascertain the material's phase. The SAED patterns of crystalline and amorphous materials differ significantly. The periodic atomic arrangement of crystalline solids produces distinct patches or rings, whereas amorphous materials lack this long-range order. As a result, the SAED pattern of an amorphous material typically resembles a diffuse halo or a broad, concentric ring rather than distinct rings or sharp points.

In the amorphous phase, when a long-range atomic structure is irregular, this diffuse pattern depicts the atoms' random dispersion. Short-range order, in which atoms may be locally grouped into small clusters but lack a recurring pattern that extends beyond a few atomic lengths, is a typical source of the broad halo. The position and intensity of this diffuse ring can be used to estimate the average interatomic distances inside the amorphous material. These SAED patterns can be used to distinguish between crystalline or polycrystalline phases and amorphous phases in materials investigation. Amorphous SAED patterns are frequently found in materials that lack crystalline structure, glasses and certain polymers [12].

2.3.4. Brunauer-Emmett-Teller surface area (BET)

BET theory is a fundamental method for characterizing the specific surface area of porous materials through nitrogen gas adsorption. Developed in 1938, by Stephen Brunauer, Paul Hugh Emmett, Edward Teller, the BET theory extends the Langmuir adsorption model by considering multilayer adsorption, which is more realistic for most solid surfaces. BET analysis measures the quantity of gas adsorbed as a function of relative pressure (P/P_0) after exposing a sample to liquid nitrogen at 77 K. The specific surface area of a material is calculated using the BET equation, which is derived from the Brunauer–Emmett–Teller theory. This calculation is based on analyzing the linear portion of the nitrogen adsorption isotherm, typically within the relative pressure (P/P_0) range of 0.05 to 0.3, where monolayer adsorption occurs [13]. The study was performed on N_2 adsorption desorption isotherm on Quantachrome Autosorb instrument **(Figure 2.6 (a))** at 77 K to get the specific surface area and pore size distribution of synthesized composites.

Hysteresis loops observed in BET adsorption-desorption isotherms provide insight into pore structure and capillary condensation behavior **(Figure 2.7)**. The International Union of Pure and Applied Chemistry (IUPAC) classifies hysteresis loops into several types (H1 to H4), each corresponding to specific pore geometries. For instance, H1 loops are associated with well-defined cylindrical pores. The H2 loop is associated with materials possessing a network of interconnected pores of varying size and shape, including "ink-bottle" pores with narrow necks and wider bodies.

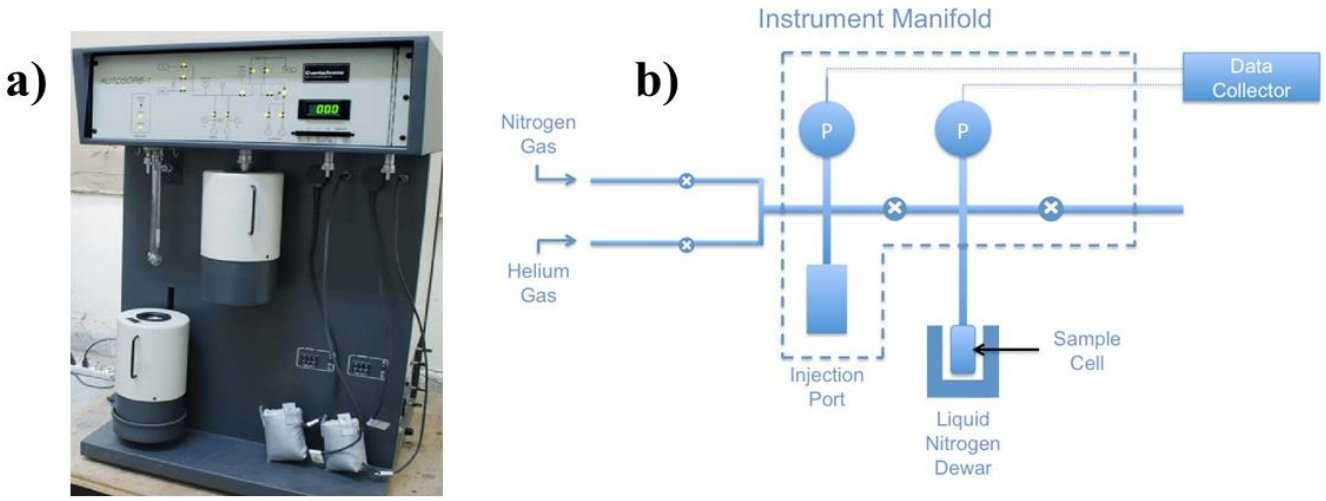

Figure 2.6 (a) BET instrument, **(b)** schematic diagram illustrating the components of Quantachrome Autosorb [14].

The desorption branch's steep nature reflects the sudden release of adsorbate from these constricted pores. H3 Hysteresis Loop lacks a limiting adsorption at high relative pressures and is typically linked to aggregates of plate-like particles or materials with slit-shaped pores. The desorption branch does not exhibit a steep drop, indicating the presence of non-rigid, open pore structures. Similar to H3, the H4 loop is associated with narrow slit-like pores but also indicates the presence of micropores. The adsorption branch often shows significant uptake at low relative pressures, characteristic of microporous materials, while the hysteresis loop itself suggests mesoporosity [15]. Materials with pore diameters ranging from 2 to 50 nm on average exhibit the Type IV isotherm [16,17].

Numerous scientific and industrial applications make extensive use of BET surface area analysis. It is essential in catalysis, as a catalyst's surface area directly affects both its activity and selectivity. Additionally, the pharmaceutical sector uses it to evaluate powder qualities that

impact medication solubility and bioavailability, and material science uses it to build adsorbents like metal-organic frameworks (MOFs) and activated carbons [18]. BET analysis also facilitates environmental applications, including the characterization of porous materials utilized for pollutant adsorption, such as biochars.

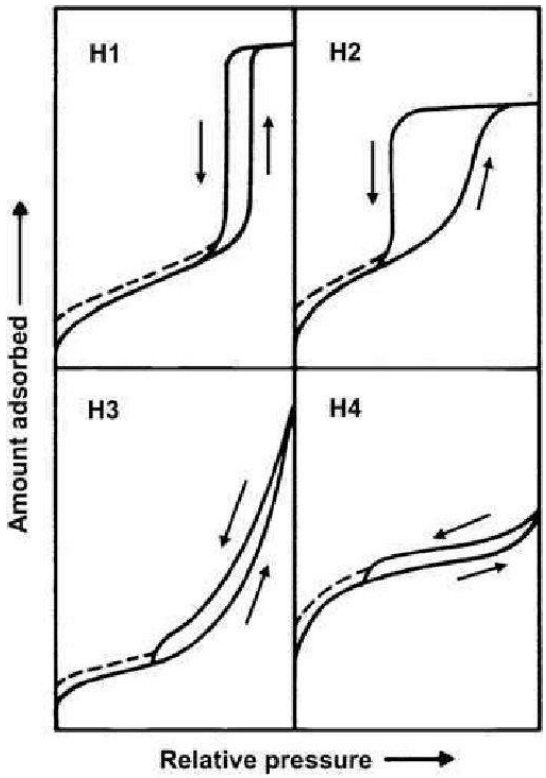

Figure 2.7. Types of hysteresis loops classified by IUPAC [19].

2.4. Elemental Analysis

2.4.1. X-ray Photoelectron Spectroscopy (XPS)

X-ray Photoelectron Spectroscopy (XPS), also known as Electron Spectroscopy for Chemical Analysis (ESCA), is a highly sensitive surface characterization technique used to determine the elemental composition, chemical states, and electronic structure of materials. XPS works

by exposing a sample to monochromatic X-rays, usually from sources of magnesium (Mg K_α, 1253.6 eV) or aluminum (Al K_α, 1486.6 eV) [20], which excite and expel core electrons from atoms at the material's surface **(Figure 2.8 (b))**. Likewise, when a sample is exposed to ultraviolet light, the photon energy will expel electrons from valence levels, revealing information about chemical bonds. This process is called UV Photoelectron Spectroscopy (UPS) [21]. The phenomenon of XPS is based on the photoelectric effect. It is possible to precisely identify elements and their oxidation states by measuring the kinetic energy of these released electrons and calculating their binding energy. XPS is especially useful for researching thin films, coatings, catalysis, corrosion layers, and contamination on various surfaces because it is intrinsically surface-sensitive, probing just the top 1–10 nm of a material, unlike bulk analysis methods.

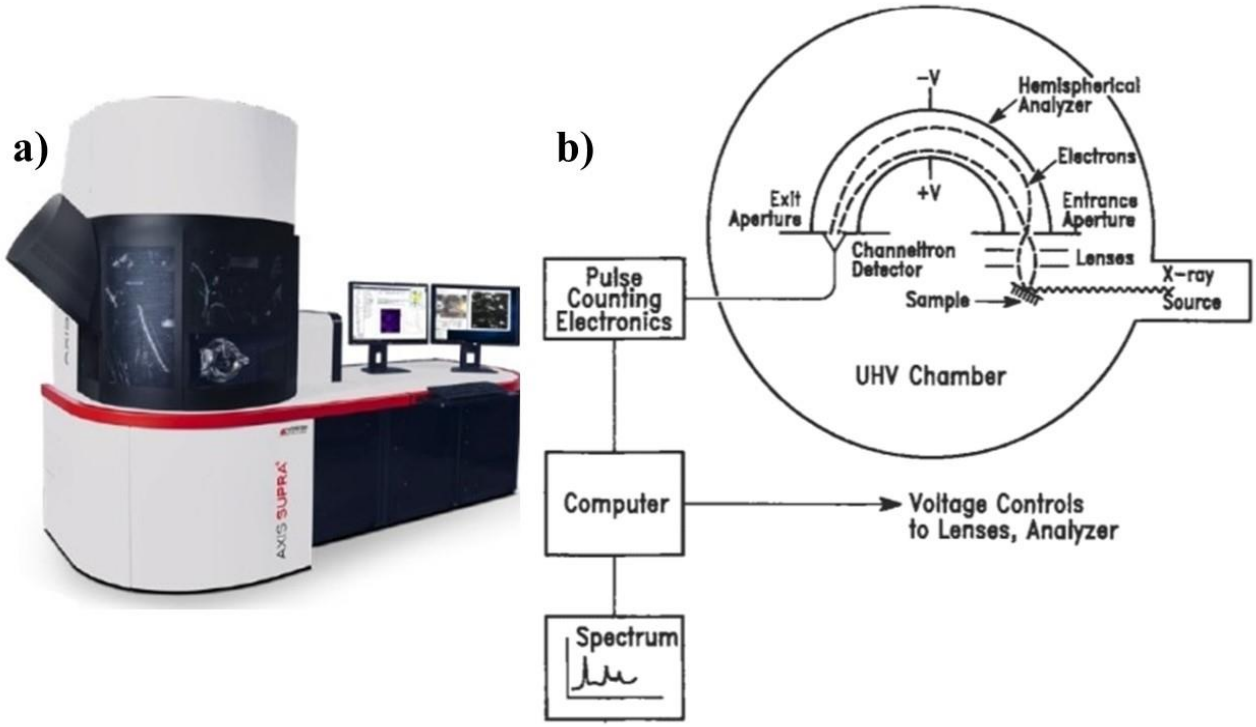

Figure 2.8 (a) XPS instrument, **(b)** schematic diagram illustrating the components of XPS system equipped with (Mg K_α) non-monochromatic X-ray source [14].

Plotting the quantity of ejected electrons against their binding energy yields an XPS spectrum. An ejected electron's kinetic energy is unique to the atom from which it came since all elements have their binding energy in electrons. Since electrons emitted from the innermost orbitals, 1s, 2s, and 2p, are least impacted by the atom's chemical environment and may therefore accurately identify the element, they are frequently considered in XPS investigations. The technique is commonly used to examine chemical bonding, oxidation states, and reaction processes in materials science, nanotechnology, semiconductors, energy storage, and medicinal research. Despite its excellent chemical specificity and quantitative analytical capabilities, XPS has a restricted spatial resolution (~10–200 μm), needs ultra-high vacuum (UHV)

conditions, and cannot detect hydrogen or helium because they lack core electrons [11]. In this thesis, XPS characterizations were performed using a Thermo Fisher Scientific XPS system equipped with (Mg Kα) non-monochromatic X-ray source with a photon energy of 1253.6 eV **(Figure 2.8 (a))**. The system was operated under ultra-high vacuum (UHV) conditions for analysis.

2.4.2. Energy Dispersive X-ray Spectroscopy (EDS)

Energy-Dispersive X-ray Spectroscopy (EDS) is a powerful analytical technique used to determine the elemental composition of materials by detecting characteristic X-rays emitted when a high-energy electron beam interacts with a sample. EDS allows for simultaneous imaging and chemical analysis at the micro to nanoscale levels when complemented by Scanning Electron Microscopy (SEM) and Transmission Electron Microscopy (TEM). The technique works on the principle that when higher-energy electrons transition to replace these vacancies left by incoming electrons ejecting inner-shell electrons from atoms, element-specific X-rays are released. A silicon drift detector (SDD) is used to detect these released X-rays, producing spectra that provide both qualitative and quantitative elemental information. The intensity of the peaks obtained by these spectra indicates the concentration of each element [22].

It is particularly useful for surface inspection and the study of thin layers or coatings, as EDS can assess the bulk concentration of elements at a narrow depth, typically between 50 and 100 nm. The accuracy and resolution of EDS have been greatly enhanced by developments in detector sensitivity, signal processing, and software, making it a vital tool for contemporary materials characterization.

2.4.3. Elemental mapping

By visualizing the spatial distribution of elements inside a sample, elemental mapping is a potent characterization tool that offers important insights into chemical heterogeneity, phase segregation, and compositional uniformity. Energy-dispersive X-ray spectroscopy (EDS), which is mostly used in combination TEM or SEM, detects distinctive X-rays that are released when a high-energy electron beam interacts with the material. Each element emits its own X-rays, which are picked up by an EDS detector and processed to provide color-coded maps that show the distribution of the elements over the scanned region.

EDS carefully scans the electron beam over the material to collect data point-by-point. This produces a thorough map that shows the locations and relative concentrations of different elements inside the sample. Elemental mapping is particularly useful for studying materials with complex compositions, such as biological tissues, metals, or ceramics. Phase boundaries, the distribution of dopants or impurities, and chemical gradients can all be seen as a result. Understanding the elemental distribution at the nanoscale is necessary to comprehend the properties of thin films, nanoparticles, and other nanoscale materials.

2.5. Electrochemical Analysis

This section provides a summary of the key components and features of an electrochemical workstation. For all electrochemical measurements in the study, we worked with the CHI-608C electrochemical analyzer/workstation, which is manufactured in the USA **(Figure 2.9 (a))**. This advanced device may be used for a variety of electrochemical processes, including Open

Circuit Potential (OCP), Electrochemical Impedance Spectroscopy (EIS), Linear Sweep Voltammetry (LSV), Cyclic Voltammetry (CV) measurements, and Tafel analysis.

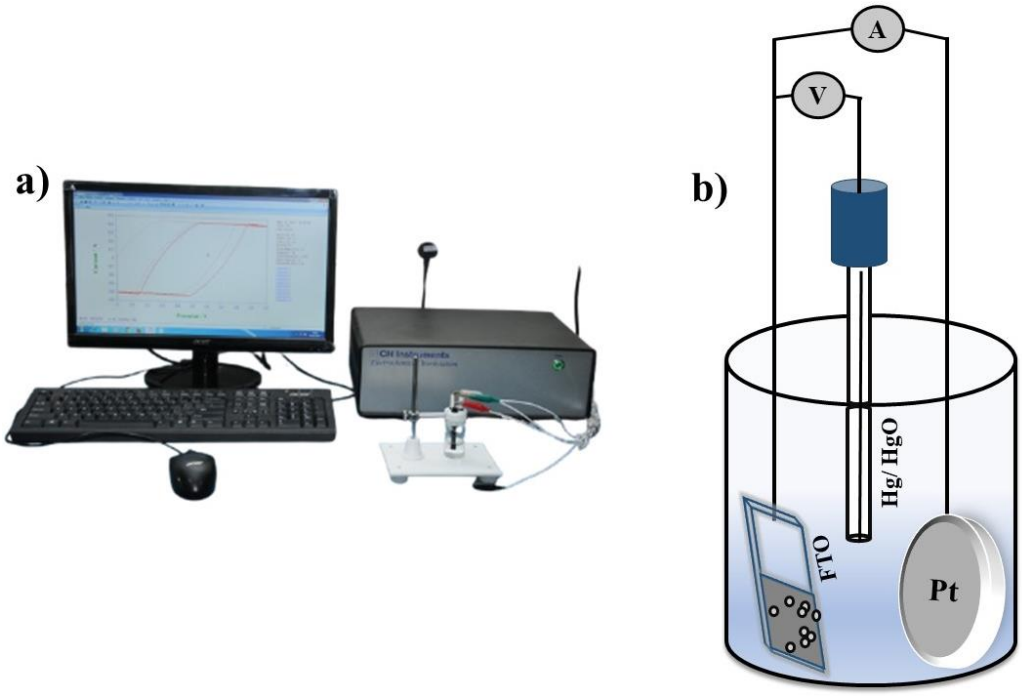

Figure 2.9 (a) CHI 608C electrochemical workstation, **(b)** electrochemical cell representation with a three-electrode setup.

It functions as a potentiostat by measuring the current between the counter and working electrodes as a function of potential. In a potentiostat, the cell potential is the controlled parameter, while the cell current is the measured one. A standard electrochemical cell setup consists of three electrodes: the working electrode (WE), where the reaction of interest occurs; the counter electrode (CE), which completes the circuit; and the reference electrode (RE), which provides a stable potential reference **(Figure 2.9 (b))**. RE is used to determine the potential of the working electrode. The ability to precisely monitor and regulate

electrochemical processes makes this arrangement ideal for investigations into redox reactions, energy storage devices.

- **Working Electrode**

Fluorine-doped tin oxide (FTO) is frequently employed as a working electrode in electrochemical and photovoltaic applications, due to its transparent conductive oxide with excellent electrical conductivity, optical transparency, and chemical stability. The output current is monitored at the working electrode, and the applied voltage serves as the controlling parameter.

- **Reference Electrode**

A reference electrode utilizing Hg/HgO in a solution of 1 M KOH was used during electrochemical measurement. When no current flows through it, its electrochemical potential ought to remain constant. Working electrode potential is measured using it.

- **Counter (Auxiliary) Electrode**

A circular platinum (Pt) foil with an 8 cm^2 area, obtained from Aldrich, was used as the counter electrode. Its high surface area ensures efficient charge transfer. It balances the redox reaction taking place at the working electrode and completes the cell circuit.

A short description of the terms, such as Open Circuit Potential (OCP), Electrochemical Impedance Spectroscopy (EIS), Linear Sweep Voltammetry (LSV), Cyclic Voltammetry (CV) measurements, and Tafel analysis, is given below.

2.5.1. Open-circuit potential (OCP)

The steady-state equilibrium potential of an electrode in the absence of an external current is represented by the open circuit potential (OCP), a basic electrochemical parameter. This method measures the natural potential difference created between an electrode and the surrounding electrolyte due to spontaneous electrochemical processes at the contact. This potential between the working electrode and a reference electrode is often measured using a high-input-impedance voltmeter, which ensures that no external current is drawn from the working electrode while the measurement is being taken. The rate of electron transport for the cathodic (reduction) and anodic (oxidation) processes on the electrode surface is equal because they are balanced at the OCP. There is no net current flow in this equilibrium due to the precise offset between the opposing reactions.

Before using methods such as chronoamperometry (CA), electrochemical impedance spectroscopy (EIS), and cyclic voltammetry (CV), OCP measurements are used as a preliminary diagnostic tool in electrochemical investigations. It assists in assessing the electrode's initial condition, observing spontaneous redox reactions, and figuring out the potential range for subsequent electrochemical tests. OCP offers important information on a material's redox activity, corrosion resistance, and thermodynamic stability and is a critical indicator of its inherent electrochemical characteristics [23].

2.5.2. Cyclic Voltammetry (CV)

CV is a potentiodynamic electrochemical study used to examine a material's or sample's redox characteristics. In CV, the working electrode's potential changes in response to an input scan

rate (mV/sec), and the output current is recorded. Cyclic voltammetry gets its name from the fact that the applied potential returns to its original input value after reaching its ultimate input value, resulting in a cyclic response of the output current. As seen in **Figure 2.10 (a)**, the cyclic voltammogram exhibits an oxidation peak (positive current) at the top half and a reduction peak (negative current) at the lower half [24]. Its purpose is to investigate the redox processes and electron transfer characteristics of an analyte in a solution or substance coated on a working electrode surface. The positions and shapes of these peaks may provide important information about the redox processes, such as the stability of the electroactive species, the reversibility of the reactions, and the kinetics of electron transfer.

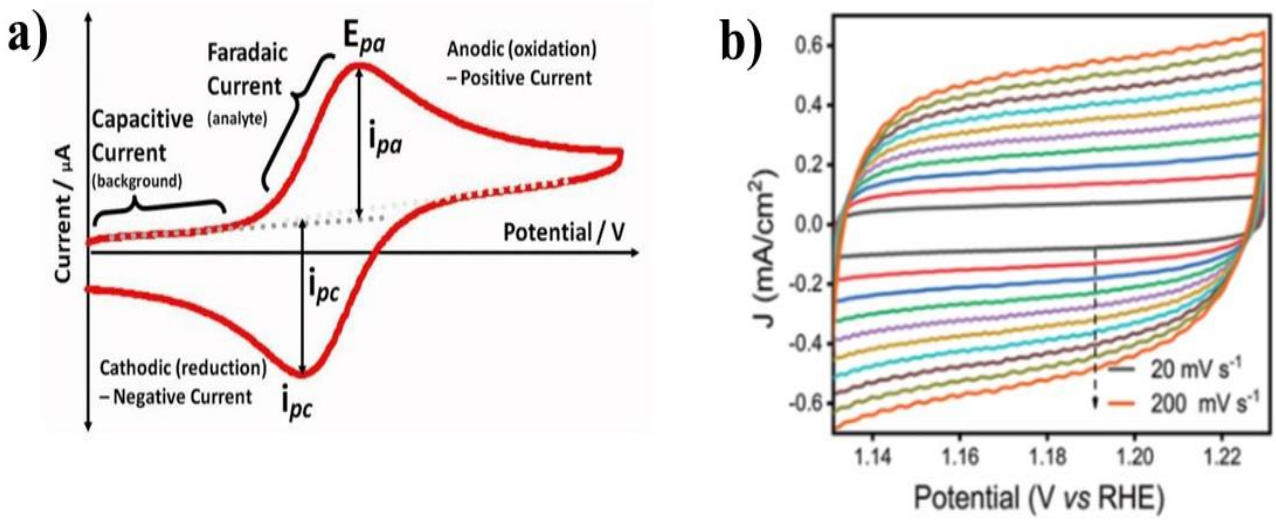

Figure 2.10 (a) Typical Cyclic Voltammogram [25], **(b)** CV in non-faradaic region [26].

One important electrochemical characteristic that indicates the voltage at which OER begins to create oxygen from water oxidation is the onset potential. The beginning of oxygen evolution at the electrode surface is indicated by the moment in a CV experiment where a

discernible Faradaic current starts to rise noticeably above the background (non-Faradaic) current. The non-Faradaic region, which occurs at lower potentials prior to the OER start, is a crucial component of CV. It is crucial for assessing electrode surface properties and inherent capacitance since there are no notable electron transfer processes in this area; rather, the current predominantly results from electrical double-layer charging and capacitive behavior **(Figure 2.10 (b))** [25].

The peak current (i_p) in a cyclic voltammogram is governed by the Randles–Ševčík equation **(Equation 2.4)**, which describes the relationship between peak current and scan rate for a reversible electrochemical process:

$$i_p = 0.4463\ nFAC\ (\ nFvD/\ RT\ )^{1/2} \qquad \textbf{(2.4)}$$

Where, i_p stands for peak current,

n stands for the number of electrons transferred in the redox process,

F is the Faraday constant,

A is the electrode area,

C is concentration,

υ is scan rate, D is diffusion coefficient,

R is gas constant,

T is the temperature in Kelvin [27].

As the scan rate rises, the peak current (i_p) rises proportionately since it is directly proportional to the square root of the scan rate.

2.5.3. Linear Sweep Voltammetry (LSV)

One popular electrochemical method for examining the redox behavior, reaction kinetics, and electrocatalytic activity of materials is linear sweep voltammetry (LSV). In LSV, the current response is measured as the electrode potential is linearly scanned throughout a predetermined voltage range. In electrochemical processes including OER, HER, and fuel cell reactions, this method is very helpful for assessing electrode reactions, onset potentials, and overpotentials.

LSV involves applying a linearly varying potential between the working and reference electrode, going from a specified lower potential limit to a higher potential limit at a given scan rate, and measuring the current that results, in contrast to CV, which scans the potential back and forth. The current response is monitored as the potential increases, and either an oxidation peak or a reduction peak is recorded based on the chosen potential range and the redox behavior of the material. LSV provides comprehensive information on the kinetics of electron transfer processes and the catalytic activity of materials under the applied conditions by focusing on a single direction of potential change. It is, therefore, an essential tool for enhancing catalysts for energy conversion applications, including batteries, fuel cells, and electrolyzers.

2.5.4. Electrochemical Impedance Spectroscopy (EIS)

A strong and adaptable electrochemical method for examining the electrical characteristics of materials, interfacial processes, and reaction kinetics in electrochemical systems is electrochemical impedance spectroscopy (EIS). EIS evaluates the system's reaction to a tiny alternating current (AC) signal throughout a broad frequency range, in contrast to traditional electrochemical techniques that apply a constant potential or current. EIS is a popular technique

in energy storage devices and electrochemical applications because of its frequency-dependent response, which offers useful information on charge transfer resistance, double-layer capacitance, diffusion processes, and overall system behavior.

The basic principle of EIS is the measurement of the corresponding AC response to a tiny sinusoidal AC voltage disturbance applied to an electrochemical system. The relationship between the applied voltage (V) and the measured current (I) defines the system's impedance (Z), which is a complex quantity given by the following **Equation 2.5**:

$$Z = V/I = Z' + Z'' \qquad \textbf{(2.5)}$$

Where, Z' (real component) represents resistive behavior, associated with charge transfer and solution resistance and Z'' (imaginary component) represents capacitive and inductive effects, related to double-layer capacitance and diffusion processes [24].

Impedance is analyzed over a broad frequency range, typically from millihertz to megahertz, allowing the separation of different electrochemical phenomena based on their characteristic time constants. A Nyquist plot is frequently used to graphically represent the test outcomes, as seen in **Figure 2.11**. The x-axis of a Nyquist plot shows the impedance's real component (Z_{real}), while the y-axis shows the imaginary component (Z_{imag}). Numerous electrochemical reactions occurring at various frequency ranges are visually represented by this type of image. The Nyquist plot frequently exhibits a semi-circular shape at higher frequencies, indicating the presence of both the uncompensated solution resistance (R_s) and charge transfer resistance (R_{ct}). The R_{ct}, which represents the kinetics of electrochemical processes like oxidation and reduction, is the resistance experienced at the electrode surface

during the electron transfer process. R_{ct} is closely correlated with the semicircle's diameter; a smaller semicircle indicates lesser resistance to charge transfer [28].

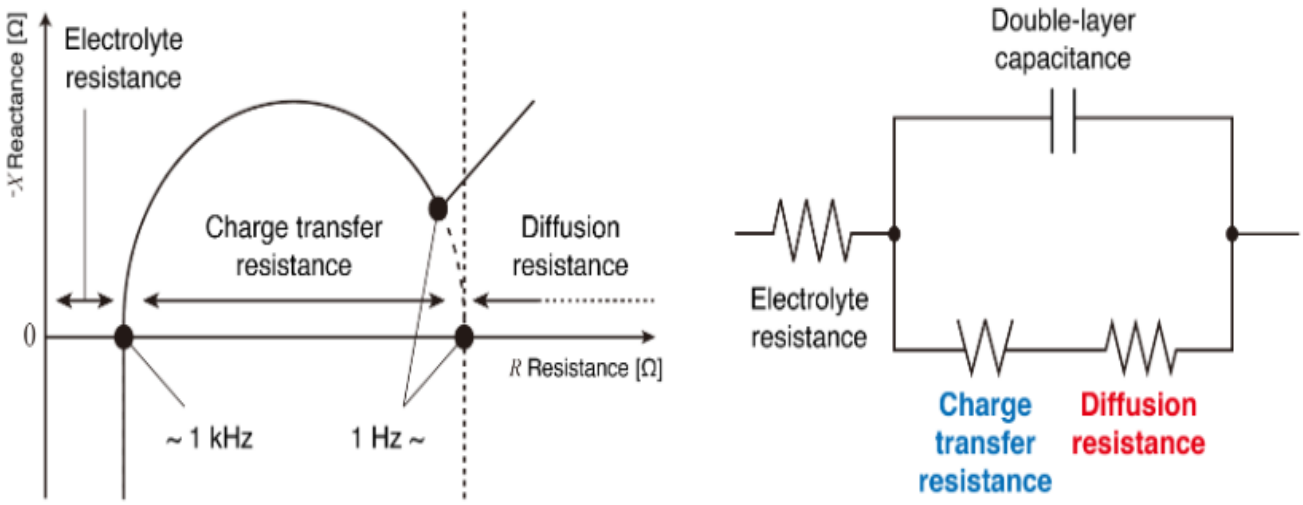

Figure 2.11 Nyquist plot and its fitted equivalent circuit [29].

The Nyquist plot often shows a linear zone at lower frequencies, which represents the system's diffusion-controlled processes. The resistance related to the mass transit or diffusion of ions within the electrolyte is shown by this linear component, which is called the Warburg impedance (W). This linear component's slope provides information about the effectiveness of mass transfer; a steeper slope denotes a more formidable ion diffusion barrier. When combined, the semicircle and the linear area provide a comprehensive view of the mass transport and charge transfer kinetics inside the electrochemical system [30].

To interpret EIS data, electrochemical systems are often modeled using equivalent electrical circuits composed of resistors (R), capacitors (C), inductors (L), and constant phase elements (CPEs). Common models include Randles circuit, and Warburg impedance. Randles

circuit represents a simple electrode system with solution resistance, charge transfer resistance, and double-layer capacitance while Warburg impedance accounts for diffusion-controlled processes, appearing as a sloped line in Nyquist plots.

2.5.5. Chronopotentiometry (CP)

In chronopotentiometry, the potential of working electrode is measured as a function of time after a fixed current is supplied to the working electrode for a specific period. This approach is used to investigate the kinetics and processes of chemical reactions in addition to electrodeposition.

Chronopotentiometry is a great way to check how stable electrochemical materials are. The potential of a stable material will either remain relatively constant or vary gradually over time, indicating that the material maintains its active sites and structural integrity with little to no deterioration. On the other hand, if the potential rises quickly or fluctuates suddenly, it can indicate surface passivation, active site loss, or electrode material degradation. This instability might be brought on by corrosion, the material disintegrating, or the accumulation of reaction intermediates that impede the process. It is a vital tool in both basic electrochemical research and real-world applications like energy storage and material characterization because of its exceptional sensitivity to diffusion-limited processes [24].

2.6. References

[1] S. Bjarnestad, O. Dahlman, Chemical compositions of hardwood and softwood pulps employing photoacoustic fourier transform infrared spectroscopy in combination with partial least-squares analysis, Anal. Chem. 74 (2002) 5851–5858. https://doi.org/10.1021/ac025926z.

[2] Q. Zhang, T. Li, J. Liang, N. Wang, X. Kong, J. Wang, H. Qian, Y. Zhou, F. Liu, C. Wei, Y. Zhao, X. Zhang, Highly wettable and metallic NiFe-phosphate/phosphide catalyst synthesized by plasma for highly efficient oxygen evolution reaction, J. Mater. Chem. A 6 (2018) 7509–7516. https://doi.org/10.1039/c8ta01334a.

[3] Skoog, D. A.; Holler, F. J.; Crouch, S. R. Principles... - Google Scholar, (n.d.).

[4] HORIBA, What is Raman Spectroscopy? - HORIBA, Ramen Imaging Spectrosc. (2020) 1–5.

[5] A. Downes, A. Elfick, Raman spectroscopy and related techniques in biomedicine, Sensors 10 (2010) 1871–1889. https://doi.org/10.3390/s100301871.

[6] L. Reimer, Scanning Electron Microscopy: Physics of Image Formation and Microanalysis, Second Edition, Meas. Sci. Technol. 11 (2000) 1826–1826. https://doi.org/10.1088/0957-0233/11/12/703.

[7] A. Billah, Investigation of multiferroic and photocatalytic properties of Li doped BiFeO3 nanoparticles prepared by ultrasonication, Diss. BANGLADESH Univ. Eng. Technol. . (2017) 23–35. http://lib.buet.ac.bd:8080/xmlui/handle/123456789/4495 (accessed April 9, 2025).

[8] R.F. Egerton, Electron Energy-Loss Spectroscopy in the Electron Microscope - R.F. Egerton - Google Books, (n.d.).

[9] Z.L. Wang, Transmission electron microscopy of shape-controlled nanocrystals and their assemblies, J. Phys. Chem. B 104 (2000) 1153–1175. https://doi.org/10.1021/jp993593c.

[10] B. Baruwati, Studies on the Synthesis, Characterization, Surface Modification and Application of Nanocrystalline Nickel Ferrite, (2015). https://www.researchgate.net/publication/49177963_Studies_on_the_Synthesis_Characterization_Surface_Modification_and_Application_of_Nanocrystalline_Nickel_Ferrite/figures?lo=1 (accessed April 9, 2025).

[11] A.E. Woods, J.W. Stirling, Transmission electron microscopy, in: Bancroft's Theory Pract. Histol. Tech. Eighth Ed., 2018: pp. 434–475. https://doi.org/10.1016/B978-0-7020-6864-5.00021-9.

[12] L. Trusilewicz, F. Fernández-Martínez, V. Rahhal, R. Talero, TEM and SAED characterization of metakaolin. Pozzolanic activity, in: J. Am. Ceram. Soc., John Wiley

& Sons, Ltd, 2012: pp. 2989–2996. https://doi.org/10.1111/j.1551-2916.2012.05325.x.

[13] S. Brunauer, P.H. Emmett, E. Teller, Adsorption of Gases in Multimolecular Layers, J. Am. Chem. Soc. 60 (1938) 309–319. https://doi.org/10.1021/ja01269a023.

[14] P. Raja, A. Barron, 2.3: BET Surface Area Analysis of Nanoparticles - Chemistry LibreTexts, Phys. Methods Chem. Nanosci. (2023). https://chem.libretexts.org/Bookshelves/Analytical_Chemistry/Physical_Methods_in_Chemistry_and_Nano_Science_%28Barron%29/02%3A_Physical_and_Thermal_Analysis/2.03%3A_BET_Surface_Area_Analysis_of_Nanoparticles (accessed April 9, 2025).

[15] K.S.W. Sing, Reporting physisorption data for gas/solid systems with special reference to the determination of surface area and porosity (Recommendations 1984), Pure Appl. Chem. 57 (1985) 603–619. https://doi.org/10.1351/pac198557040603.

[16] P. Arunachalam, M.N. Shaddad, A.S. Alamoudi, M.A. Ghanem, A.M. Al-Mayouf, Microwave-assisted synthesis of Co3(PO4)2 nanospheres for electrocatalytic oxidation of methanol in alkaline media, Catalysts 7 (2017). https://doi.org/10.3390/catal7040119.

[17] E. Okon, H. Shehu, Evaluation and Characterisation of Composite Mesoporous Membrane for Lactic Acid and Ethanol Esterification, J. Adv. Chem. Eng. 06 (2016). https://doi.org/10.4172/2090-4568.1000147.

[18] J. Rouquerol, F. Rouquerol, P. Llewellyn, G. Maurin, K.S.W. Sing, Adsorption by Powders and Porous Solids: Principles, Methodology and Applications: Second Edition, 2013. https://doi.org/10.1016/C2010-0-66232-8.

[19] M.D. Donohue, G.L. Aranovich, Adsorption hysteresis in porous solids, J. Colloid Interface Sci. 205 (1998) 121–130. https://doi.org/10.1006/jcis.1998.5639.

[20] C.R. Brundle, Photoelectron Spectroscopy: An Introduction to Ultraviolet Photoelectron Spectroscopy in the Gas Phase, Phys. Bull. 26 (1975) 129–130. https://doi.org/10.1088/0031-9112/26/3/044.

[21] L. Armelao, D. Barreca, G. Bottaro, S. Gross, A. Gasparotto, C. Maragno, E. Tondello, A. Zattin, Introduction to XPS Studies of Metal and Metal-oxide Nanosystems, Surf. Sci. Spectra 10 (2003) 137–142. https://doi.org/10.1116/11.20050199.

[22] M. Scimeca, S. Bischetti, H.K. Lamsira, R. Bonfiglio, E. Bonanno, Energy dispersive X-ray (EDX) microanalysis: A powerful tool in biomedical research and diagnosis, Eur. J. Histochem. 62 (2018) 89–99. https://doi.org/10.4081/ejh.2018.2841.

[23] L.R. Bard, Allen J., Faulkner, Fundamentals and Applications Plasmonics : Fundamentals and Applications, 2001. https://books.google.com/books?hl=en&lr=&id=Sct6EAAAQBAJ&oi=fnd&pg=PR21&ots=QV3mtaJ2QS&sig=WpR4J4YmgS8Ty7LGdhYY4R8tPNI (accessed May 6, 2024).

[24] L.R. Bard, Allen J., Faulkner, Fundamentals and Applications Plasmonics : Fundamentals and Applications, 2001.

[25] V. Climent, J.M. Feliu, Cyclic voltammetry, in: Encycl. Interfacial Chem. Surf. Sci. Electrochem., Elsevier, 2018: pp. 48–74. https://doi.org/10.1016/B978-0-12-409547-2.10764-4.

[26] G. Solomon, A. Landström, R. Mazzaro, M. Jugovac, P. Moras, E. Cattaruzza, V. Morandi, I. Concina, A. Vomiero, NiMoO4@Co3O4 Core–Shell Nanorods: In Situ Catalyst Reconstruction toward High Efficiency Oxygen Evolution Reaction, Adv. Energy Mater. 11 (2021). https://doi.org/10.1002/aenm.202101324.

[27] O.A. González-Meza, E.R. Larios-Durán, A. Gutiérrez-Becerra, N. Casillas, J.I. Escalante, M. Bárcena-Soto, Development of a Randles-Ševčík-like equation to predict the peak current of cyclic voltammetry for solid metal hexacyanoferrates, J. Solid State Electrochem. 23 (2019) 3123–3133. https://doi.org/10.1007/s10008-019-04410-6.

[28] A. Soni, S. Kumar Maurya, M. Malviya, D. Tiwary, Exploring the synergistically enhanced activity of novel α-MnSe/ppy composite for superior OER catalyst in alkaline medium, J. Electroanal. Chem. 972 (2024) 118640. https://doi.org/10.1016/j.jelechem.2024.118640.

[29] T. Tools, Nyquist Plot for Impedance Measurement of Lithium-ion Batteries, Https://Www.Hioki.Com/in-En/Learning/Electricity/Nyquist.Html (2021) 1–8. https://www.hioki.com/us-en/learning/electricity/nyquist.html (accessed October 17, 2024).

[30] R. Vedalakshmi, V. Saraswathy, H.W. Song, N. Palaniswamy, Determination of diffusion coefficient of chloride in concrete using Warburg diffusion coefficient, Corros. Sci. 51 (2009) 1299–1307. https://doi.org/10.1016/j.corsci.2009.03.017.